Research on Externally Pressurized Porous Thrust Gas Bearing with Supply Hole

By

Haruo MORI* and Yasunao YOKOTA**

(Received March 19, 1982)

Abstract

In this research, the characteristics of an externally pressurized porous circular thrust bearing with a supply hole on its center is investigated. In the analysis, the hypothesis of equivalent film thickness is applied to the flow in the porous media. Dynamic performances are obtained theoretically for various controllable parameters. The theoretical results show a comparatively good conformity with the experimental results. It is proved that, by providing a supply hole, desirable perfornamces can be obtained over wide operating conditions. The results attained in this research may allow the designers to get optimal design conditions.

Nomenclature

A_0 $=2\pi r_s h$, minimum sectional area at supply hole
B damping coefficient, dimensionless
c damping coefficient
C_D discharge coefficient
f frequency
H_r $=h'/h_0$, gap, dimensionless
h local bearing gap
h_0 gap in equilibrium
K stiffness, dimensionless
k permeability coefficient
k^* stiffness
m mass
$\dot{m}$ mass flow rate
P $=p/p_a$, pressure, dimensionless
p local pressure
R $=r/r_0$, radius or radial coordinate, dimensionless

* Department of Mechanical Engineering
** Kobe Steel Works, Ltd.

$\boldsymbol{R}$ gas constant
r_0 radius of bearing
r_1 radius of porous portion
T gas temperature
t thickness of porous bushing
$\hat{t}$ time
u flow velocity in r direction
v flow velocity in z direction
W load capacity, dimensionless
w load capacity
z axial coordinate
Γ eq. (2.16), feeding parameter, dimensionless
γ permeability ratio
δ logarithmic decrement
θ angular coordinate
ϵ amplitude, dimensionless
η effective restricting length
κ ratio of specific heat
λ $=\dfrac{12\mu\omega}{p_a}\left(\dfrac{r_0}{h_0}\right)^2$, squeeze number, dimensionless
μ coefficient of viscosity
ρ density of gas
σ porosity coefficient of porous media
τ $=\omega\hat{t}$, time, dimensionless
ϕ speed of gas through inherent orifice
ψ $=-R_s \ln R_s$, correction factor for dispersion effect
ω angular velocity

Subscripts

a ambient
b outlet
s supply or supply pressure
$'$ in assumed film with equivalent thickness
$''$ in assumed vertical capillary passage

1. Introduction

Externally pressurized porous gas bearings have much superior characteristics due to the multiplicity of the feeding holes of the porous media, which spread the supply pressure effectively over the bearing surface.

Several papers have reported on the dynamic performances of the conventional porous thrust bearing. However, in the application of a small gap, the range of which gives the optimum designing point is restricted within narrow limits. This hybrid-type bearing which has a porous bearing surface and a central supply hole is proposed to improve this defect by adding the effect of the inherently compensated restrictor.

The hypothesis of equivalent film thickness[1,2] is applied to the gas flow in the porous media. This hypothesis, in which the flow in the porous bushing is represented by a flow through an assumed thin layer, can make it easy to accomplish the theoretical treatment.

This paper also refers to the determination of the parameters which characterize the flow profile in the porous media, taking into account the loading effect of the ground surface.

2. Theoretical Study

2.1 Theoretical Analysis

Fig. 1 shows the bearing analyzed here. The compressed gas flows through both the porous media and the inherent restictor from a central supply hole into bearing gap. Fig. 2 shows the theoretical model of the gas flow for the analysis, introducing the equivalent film thickness h' and the effective restricting length η.

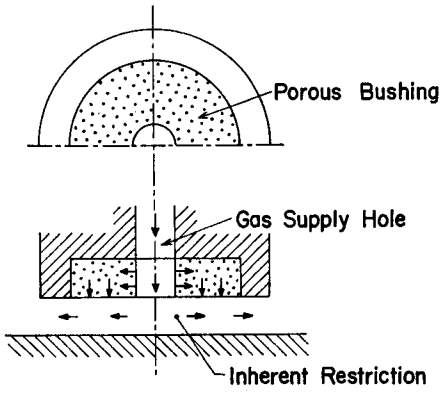

Fig. 1. Schematic diagram of the bearing.

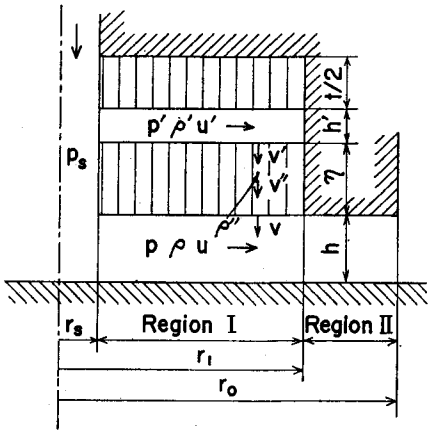

Fig. 2. Analytical flow model.

Assumptions

In this analysis, the following assumptions are made:

1. Gas behaves as a Newtonian fluid, and its viscosity is independent of temperature or pressure.

2. Gas flow in the bearing gap is characterized as a fully developed laminar viscous flow.
3. The flow is isothermal and the perfect gas law is adoptable throughout the bearing.
4. Circumferential flow is negligible.
5. Bearing gap is small enough compared with its radius, so that the pressure of the gap normal to the bearing surface is constant along the z direction.
6. Gas flow through the porous media follows Darcy's law, and the hypothesis of equivalent film thickness[1,2] is applied.

Basic Equations

The governing equations in the bearing gap are treated separately, namely Region I for the gap facing the porous wall and Region II for that facing the impermeable wall.

By using assumption 6, the vertical velocity, v'' in the restricting capillary passage can be written;

$$v'' = -\frac{k}{\mu}\frac{\partial p''}{\partial z} \tag{2.1}$$

and the assumption of a viscous flow yields

$$u = -\frac{h^2}{12\mu}\frac{\partial p}{\partial r} \tag{2.2}$$

$$u' = -\frac{h'^2}{12\mu}\frac{\partial p'}{\partial r} \tag{2.3}$$

where h' is the equivalent film thickness defined as

$$h' = \sqrt[3]{12kt} \tag{2.4}$$

k: permeability coefficient

t: actual thkickness of the porous bushing

Eq. (2.1) with assumption 3 ($p=\rho RT$) can be integrated once to yield

$$\rho v = \frac{1}{2RT}\cdot\frac{h'^3}{12\mu t}\cdot\frac{p'^2-p^2}{\eta} (= \rho' v' = \rho'' v'') \tag{2.5}$$

where η is the effective restricting length defined as

$$\eta = \left(\gamma - \frac{1}{2}\right)t \tag{2.6}$$

γ represents the permeability ratio of the original porous metal and the ground

one.

The continuity equation at the bearing gap (Region I) is given as

$$\rho v = h\frac{\partial}{r\partial r}(r\cdot\rho u)+\frac{\partial(\rho h)}{\partial \hat{t}} \tag{2.7}$$

By making use of eqs. (2.2) and (2.5), eq. (2.7) is rewritten as

$$\frac{1}{r}\frac{\partial}{\partial r}\left[r\cdot\frac{h^3}{12\mu}p\frac{\partial p}{\partial r}\right]=\frac{\partial(ph)}{\partial \hat{t}}-\frac{h'^3}{24\mu t\eta}(p'^2-p^2) \tag{2.8}$$

Similarly, the continuity equations in the porous media and in the bearing gap (Region II) also yield

$$\frac{1}{r}\frac{\partial}{\partial r}\left[r\frac{h'^3}{12\mu}p'\frac{\partial p'}{\partial r}\right]=\sigma t\frac{\partial p'}{\partial \hat{t}}+\frac{h'^3}{24\mu t\eta}(p'^2-p^2) \tag{2.9}$$

$$\frac{1}{r}\frac{\partial}{\partial r}\left[r\frac{h^3}{12\mu}p\frac{\partial p}{\partial r}\right]=\frac{\partial(ph)}{\partial \hat{t}} \tag{2.10}$$

Non-dimensionalization is achieved by defining

$$R=\frac{r}{r_0},\quad P=\frac{p}{p_a},\quad H_r=\frac{h'}{h_0},\quad \tau=\omega\hat{t},\quad \lambda=\frac{12\mu\omega}{p_a}\left(\frac{r_0}{h_0}\right)^2,$$

$$G_1=\frac{r_0^2}{t\eta},\quad J_1=\frac{H_r^3\cdot G_1}{2},\quad G_2=\frac{\sigma t}{h'},\quad J_2=\frac{G_2}{H_r^2}$$

where λ is the dimensionless squeeze number, and $\lambda=0$ corresponds to the static case.

Then, eqs. (2.8)–(2.10) are reqwritten as

$$\frac{1}{R}\frac{\partial}{\partial R}\left[RH_r^3P\frac{\partial P}{\partial R}\right]=\lambda\frac{\partial(PH_r)}{\partial\tau}-J_1(P'^2-P^2) \tag{2.11}$$

$$\frac{1}{R}\frac{\partial}{\partial R}\left[RP'\frac{\partial P'}{\partial R}\right]=\lambda J_2\frac{\partial P'}{\partial\tau}+\frac{G_1}{2}(P'^2-P^2) \tag{2.12}$$

$$\frac{1}{R}\frac{\partial}{\partial R}\left[RH^3P\frac{\partial P}{\partial R}\right]=\lambda\frac{\partial(PH_r)}{\partial\tau} \tag{2.13}$$

Eqs.(2.11)–(2.13) are the modified Reynolds equations to be solved.

Boundary Conditions

(I) Mass continuity at the film inlet of the inherent restrictor

Under the assumption of an isentropic change,

$$\dot{m}_{in}=\frac{C_DA_0}{\sqrt{RT}}p_s\phi \tag{2.14}$$

$$\dot{m}_{out} = \oint_{r_s} -\frac{h^3}{12\mu RT} p \frac{\partial p}{\partial r} dS \tag{2.15}$$

where A_0 is the minimum cross sectional area, $2\pi r_s h$.

These two equations are equated to yield

$$\frac{\partial P^2}{\partial R} = \frac{\Gamma P_s \phi}{\psi} \tag{2.16}$$

where

$$\Gamma = \frac{-24\mu C_D r_s \sqrt{RT}}{p_a h_0^2} ln\left(\frac{r_s}{r_0}\right), \quad \Psi = -R_s ln R_s$$

Γ is called the feeding parameter and represents the restriction ratio of the inherent orifice and the bearing gap. ϕ is the flow function of the nozzle shown in Table 1.

Table 1.

(1) ε^0 order

Basic Equations

$$\frac{1}{R}\frac{d}{dR}\left[R\frac{dP_0^2}{dR}\right]=G_1(P_0^2-P_{01}^2)$$

$$\frac{1}{R}\frac{d}{dR}\left[R\frac{dP_{01}^2}{dR}\right]=-2J_1(P_0^2-P_{01}^2)$$

$$\frac{1}{R}\frac{d}{dR}\left[R\frac{dP_{02}^2}{dR}\right]=0$$

Boundary Conditions

$$\left.\frac{dP_{01}^2}{dR}\right|_{R=R_s}=\frac{\Gamma P_s\phi_0}{\psi}$$

$$P_0|_{R=R_s}=P_s$$

$$P_{01}|_{R=R_1}=P_{02}|_{R=R_1}$$

$$\left.\frac{dP_0}{dR}\right|_{R=R_1}=0$$

$$P_{02}|_{R=1}=1$$

(2) $\varepsilon \sin\tau$

Basic Equations

$$\frac{1}{R}\frac{d}{dR}\left[R\frac{dP_0P_1}{dR}\right]=-\lambda J_2P_2+G_1(P_0P_1-P_{01}P_{11})$$

$$\frac{1}{R}\frac{d}{dR}\left[R\frac{dP_{01}P_{11}}{dR}\right]=J_1\{3(P_0^2-P_{01}^2)-2(P_0P_1-P_{01}P_{11})\}-\lambda P_{21}$$

$$\frac{1}{R}\frac{d}{dR}\left[R\frac{dP_{02}P_{12}}{dR}\right]=-\lambda P_{22}$$

Boundary Conditions

$$\left.\frac{dP_{01}P_{11}}{dR}\right|_{R=R_s}=-\frac{\Gamma P_s\phi_0}{\psi}\left[1+\frac{A}{P_m}(P_{01}P_{11})\right]_{R=R_s}$$

$$P_1|_{R=R_s}=0$$

$$P_{11}|_{R=R_1}=P_{12}|_{R=R_1}$$

$$\left.\frac{dP_1}{dR}\right|_{R=R_1}=0$$

$$P_{12}|_{R=1}=0$$

Table 1 continued

(3) $\varepsilon \cos \tau$

Basic Equations

$$\frac{1}{R}\frac{d}{dR}\left[R\frac{dP_0P_2}{dR}\right]=\lambda J_2P_1+G_1(P_0P_2-P_{01}P_{21})$$

$$\frac{1}{R}\frac{d}{dR}\left[R\frac{dP_{01}P_{21}}{dR}\right]=\lambda(P_{01}+P_{11})-2J_1(P_0P_2-P_{01}P_{21})$$

$$\frac{1}{R}\frac{d}{dR}\left[R\frac{dP_{02}P_{22}}{dR}\right]=\lambda(P_{02}+P_{12})$$

Boundary conditions

$$\left.\frac{dP_{01}P_{21}}{dR}\right|_{R=R_s}=-\frac{\Gamma P_s\phi_0}{\psi}\left[\frac{A}{P_m}(P_{01}P_{21})\right]_{R=R_s}$$

$$P_2|_{R=R_s}=0$$

$$P_{21}|_{R=R_1}=P_{22}|_{R=R_1}$$

$$\left.\frac{dP_2}{dR}\right|_{R=R_1}=0$$

$$P_{22}|_{R=1}=0$$

where

$$\phi=\begin{cases}\sqrt{\dfrac{2\kappa}{\kappa-1}(\gamma^{2/\kappa}-\gamma^{(\kappa+1)/\kappa})} & \text{for } \gamma\geq\left(\dfrac{2}{\kappa+1}\right)^{\kappa/(\kappa-1)}\\ \sqrt{\dfrac{2\kappa}{\kappa+1}\left(\dfrac{2}{\kappa+1}\right)^{2/(\kappa-1)}} & \text{for } \gamma\leq\left(\dfrac{2}{\kappa+1}\right)^{\kappa/(\kappa-1)}\end{cases}$$

$$A=\begin{cases}\dfrac{1}{4P_s}\cdot\left(\dfrac{\dfrac{\kappa+1}{\kappa}\gamma^{1/\kappa}-\dfrac{2}{\kappa}\gamma^{(2-\kappa)/\kappa}}{\gamma^{2/\kappa}-\gamma^{(\kappa+1)/\kappa}}\right) & \text{for } \gamma\geq\left(\dfrac{2}{\kappa+1}\right)^{\kappa/(\kappa-1)}\\ 0 & \text{for } \gamma\leq\left(\dfrac{2}{\kappa+1}\right)^{\kappa/(\kappa-1)}\end{cases}$$

$$\gamma=\frac{P}{P_s}$$

ϕ is perturbed as

$$\phi=\phi_0+\varepsilon\sin\tau\cdot\left.\frac{\partial\phi}{\partial P}\right|_{P=P_0}P_1+\varepsilon\cos\tau\cdot\left.\frac{\partial\phi}{\partial P}\right|_{P=P_0}P_2$$

$$P_m=P_0|_{R=R_s}$$

Other boundary conditions are shown below.

$$\text{(II)}\qquad P'=P_s \quad \text{at} \quad R=R_s \tag{2.17}$$

$$\text{(III)}\qquad P(\text{region I})=P(\text{region II}) \quad \text{at} \quad R=R_1 \tag{2.18}$$

$$\text{(IV)}\qquad \frac{dP'}{dR}=0 \quad \text{at} \quad R=R_1 \tag{2.19}$$

$$\text{(V)}\qquad P=1 \quad \text{at} \quad R=1 \tag{2.20}$$

Linearization

Perturbation is carried out in evaluating the dynamic performances. The following assumptions can be made,

$$H_r=1+\varepsilon\sin\tau \tag{2.21}$$

$$P=P_{01}+\varepsilon(P_{11}\sin\tau+P_{21}\cos\tau)\text{: region I} \tag{2.22}$$

$$P=P_{02}+\varepsilon(P_{12}\sin\tau+P_{22}\cos\tau)\text{: region II} \tag{2.23}$$

$$P' = P_0 + \varepsilon(P_1 \sin \tau + P_2 \cos \tau) \tag{2.24}$$

Then, eqs. (2.11)–(2.13) and boundary conditions (2.16)–(2.20) are rewritten, as shown in Table 1. For the first set of equations, analytical solutions are available to give static characteristics. The remaining 2 sets of equations are solved numerically.

The dimensionless stiffness and damping coefficient are obtained by integrating the perturbed pressure over the bearing surface.

$$K = \frac{k^* h_0}{\pi r_0^2 p_a} = -\frac{1}{\pi}\left[\int_0^{2\pi}\int_{R_s}^{R_1} P_{11} R dR d\theta + \int_0^{2\pi}\int_{R_1}^{1} P_{12} R dR d\theta\right] \tag{2.25}$$

$$B = \frac{c h_0 \omega}{\pi r_0^2 p_a} = -\frac{1}{\pi}\left[\int_0^{2\pi}\int_{R_s}^{R_1} P_{21} R dR d\theta + \int_0^{2\pi}\int_{R_1}^{1} P_{22} R dR d\theta\right] \tag{2.26}$$

where k^* and c represent the actual stiffness and the actual damping coefficient respectively.

2.2 Theoretical Results and Discussion

In this section, the effects of various controllable parameters on the dynamic stiffness and the damping coefficients are examined. The parameters are: dimensionless gap H_r, supply pressure P_s, permeability coefficient k, permeability ratio γ, proportion of the porous wall R_1, radius of the supply hole R_s, and squeeze number λ. Other dimensions used in these results are: $t=0.5$ cm, $r_0=2.8$ cm and $\sigma=0.3$.

(1) Effect of the supply pressure, P_s (Figs. 3,4)

A higher supply pressure results in a higher K and increases the value of H_r which gives the peak point on the left-hand side. Two peaks can be observed, the one on the left being dependent on the existence of the inherent restrictor and the other on the right being the porous restrictor.

(2) Effect of the permeability coefficient, k (Figs. 5,6)

One of the interesting features seen from these relations is that the values of H_r, which give the right-hand peak of K, remain constant regardless of the variation of k. It means that a smaller permeability coefficient is desirable for a smaller gap, because the decreasing permeability corresponds to the reduction of the equivalent film thickness.

(3) Effect of the permeability ratio, γ (Figs. 7,8,9,10)

From these results, it becomes clear that comparatively low values of γ are likely to give negative damping coefficients, and high values of γ have less effects on B. It is of interest that H_r, which gives the right-hand peak of K, increases with an increasing γ. One may conclude that if a permeability coefficient is

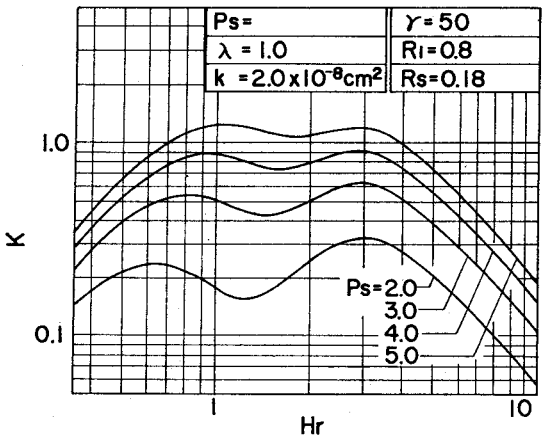

Fig. 3. Effect of supply pressure on *K*.

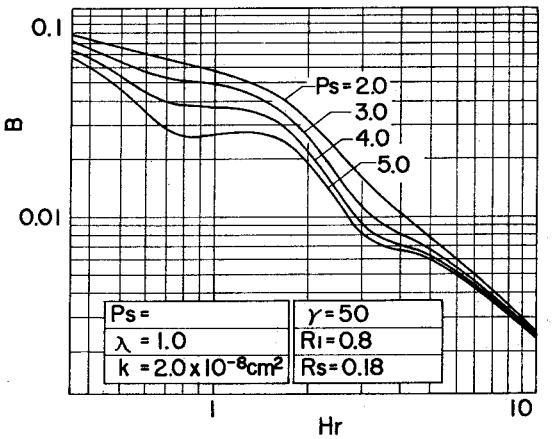

Fig. 4. Effect of supply pressure on *B*.

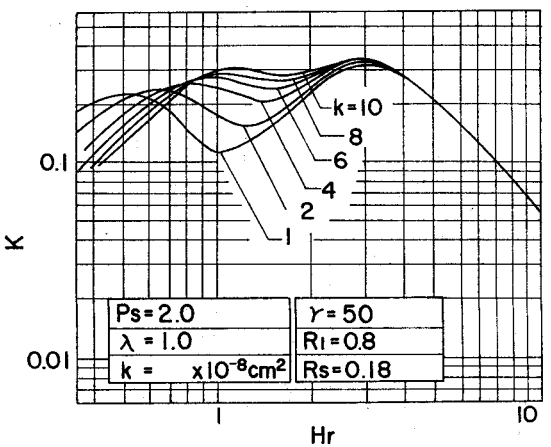

Fig. 5. Effect of permeability coefficient on *K*.

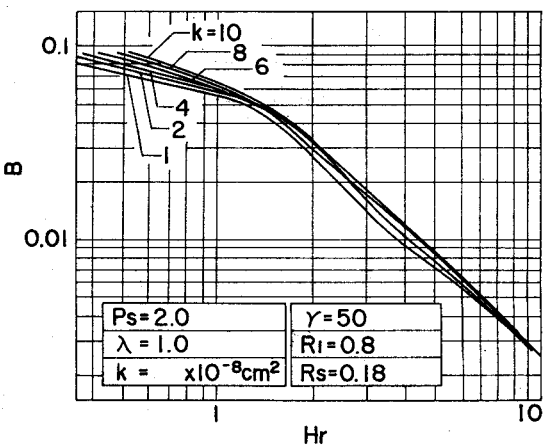

Fig. 6. Effect of permeability coefficient on *B*.

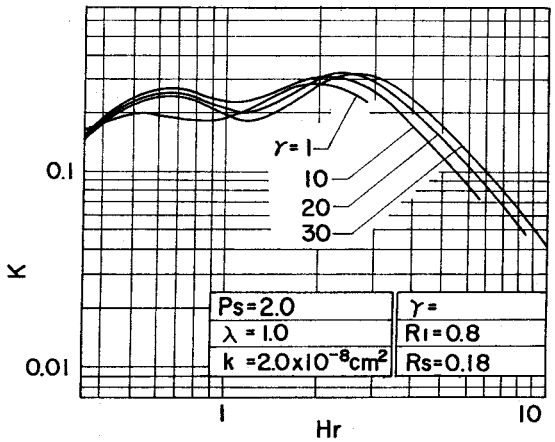

Fig. 7. Effect of permeability ratio on K, ((i).

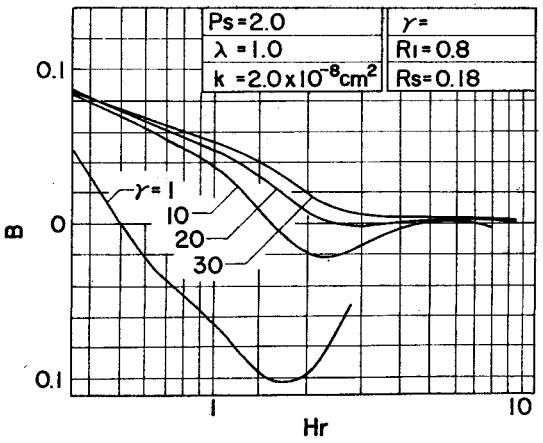

Fig. 8. Effect of permeability ratio on B, (i).

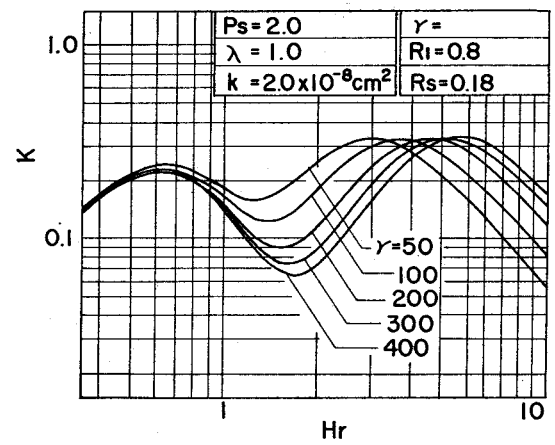

Fig. 9. Effect of permeability ratio on K, (ii).

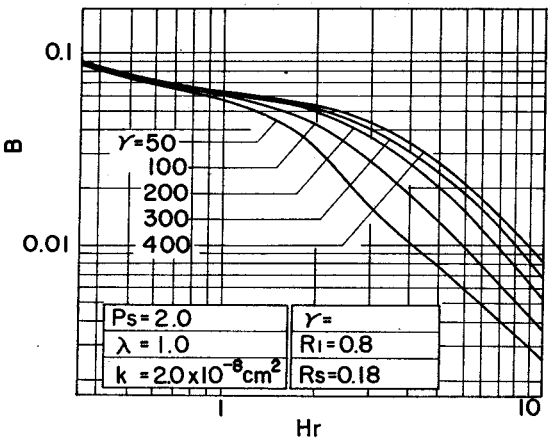

Fig. 10. Effect of permeability ratio on B, (ii).

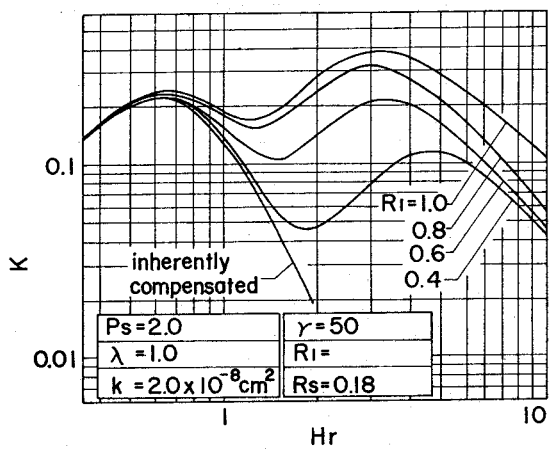

Fig. 11. Effect of R_1 on K.

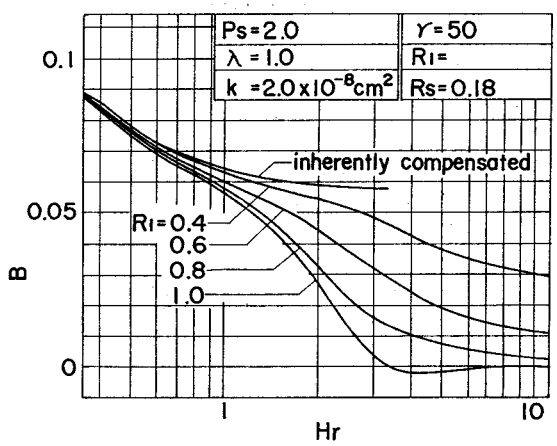

Fig. 12. Effect of R_1 on B.

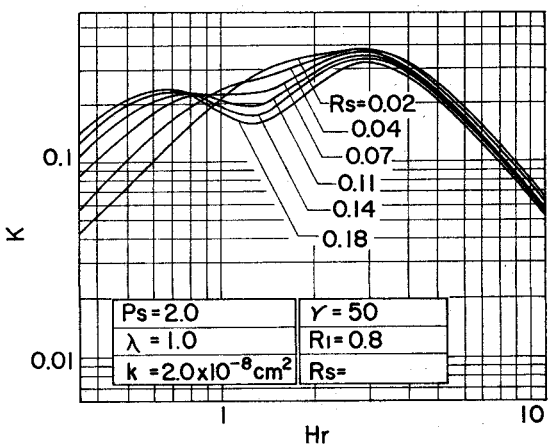

Fig. 13. Effect of R_s on K.

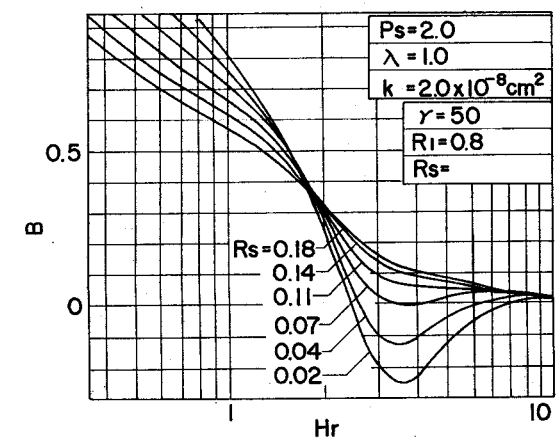

Fig. 14. Effect of R_s on B.

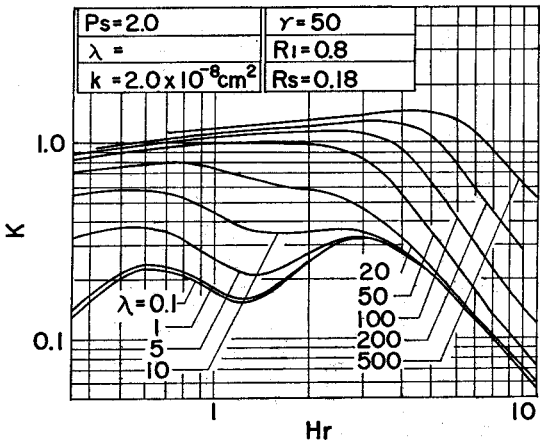

Fig. 15. Effect of squeeze number on K, (i).

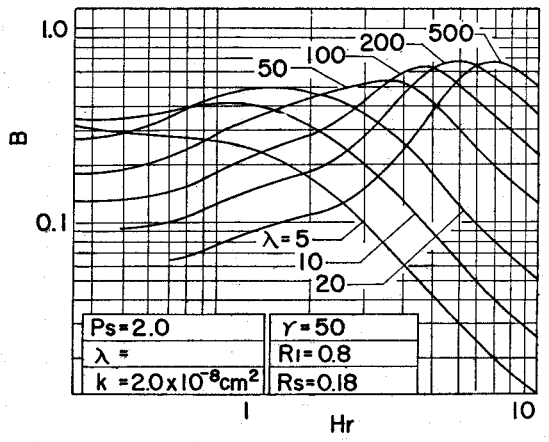

Fig. 16. Effect of squeeze number on B, (i).

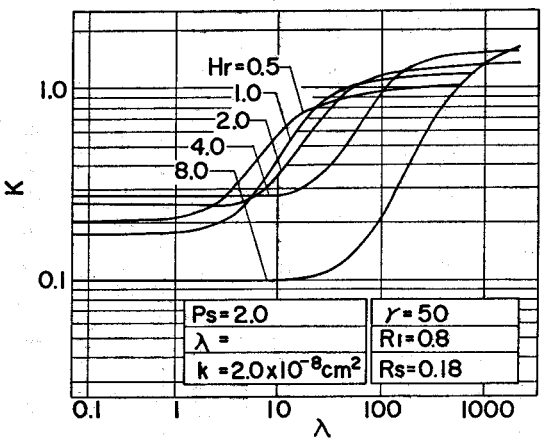

Fig. 17. Effect of squeeze number K, on (ii).

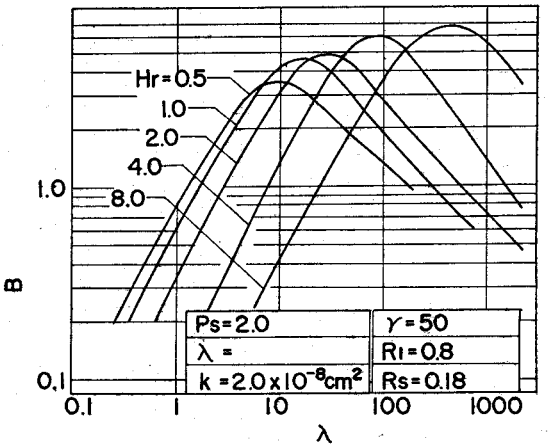

Fig. 18. Effect of squeeze number on B, (ii).

given, a desirable performance is obtained by employing a high value of the permeability ratio.

(4) Effect of the radial proportion of the porous wall, R_1 (Figs. 11,12)

R_1 is the dimensionless radius of the porous wall which occupies in the whole bearing surface, and the $R_1=0.18$ case corresponds to the inherent restrictor. The diminishing value of R_1 reduces K and the effect becomes more significant as H_r increases. It is shown, however, that a high value of R_1 may cause instability.

(5) Effect of the radius of the supply hole, R_s (Figs. 13,14)

The value of H_r, which gives the left-hand peak of K increases expectedly as the supply hole becomes small. It should also be pointed out that a small value of r_s is likely to give a negative damping coefficient. This accounts for the fact that the existence of the porous bushing in the inherently restricted bearing substantially causes instability.

(6) Effect of the squeeze number, λ (Figs. 15,16,17,18)

One may find little variation of K for comparatively small values of λ, which describes that the $\lambda=1.0$ case nearly corresponds to the static condition where the effect of the squeeze action is less dominant. K, for the small value of H_r, first increases with an increasing λ, and then, for the relatively high value of H_r, K increases with an increasing λ. As for B, its peak is observed for respective values of H_r. The value of λ which gives the peak of B increases as H_r increases. It is noted that, for comparatively higher values of H_r, the effects of λ on K and B become more significant.

As mentioned above, some criteria in designing this hybrid-type bearing are developed. One should adopt such parameters as to give a high stiffness and positive damping coefficient for a required operating condition.

3. Experimental Study

3.1 Examination on Gas Flow through Porous Media

The gas flow in the porous media should be treated deliberately. In this section, two parameters which characterize the profile of the gas flow are examined. The permeability coefficient of each porous metal is obtained first, and then the porous metal is set in the bearing. The permeability ratio is obtained after the bearing surface is ground. [Appendixes]

Permeability coefficient, k

The size of the pores and the quantity of porosity determine the permeability coefficient of the porous media. Darcy's law is suitable for the flow of the viscous fluids. For the gas flow, however, the permeability coefficient decreases as the

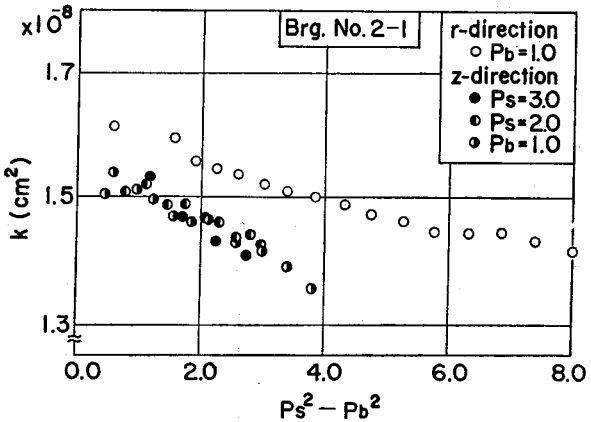

Fig. 19. Measured permeability coefficient, (i).

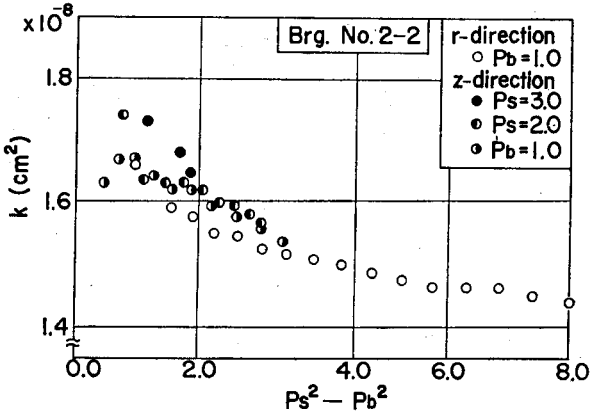

Fig. 20. Measured permeability coefficient, (ii).

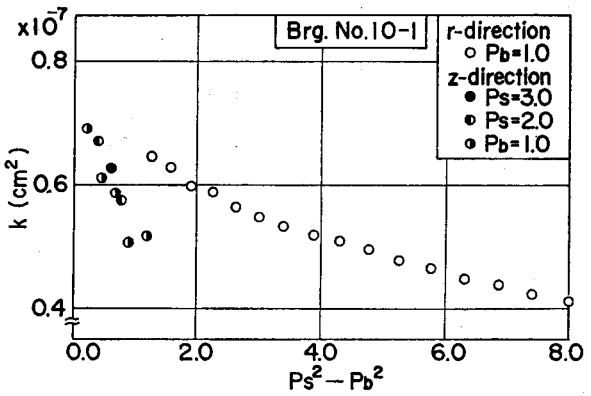

Fig. 21. Measured permeability coefficient, (iii).

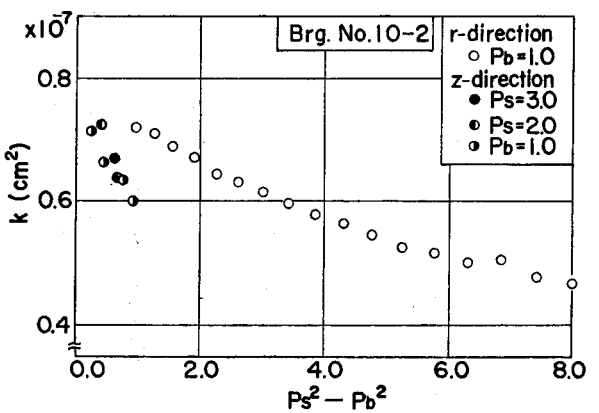

Fig. 22. Measured permeability coefficient, (iv).

mass flow rate increases. This must be because the inertial effects become significant with the increasing mass flow rate.

Figs. 19–22 show the relations between permeability coefficient and pressure for both r and z directions. Variations of the permeability coefficients for Brg. No. 2–1 and 2–2 are at most 20 percent and about 30 percent for Brg. No. 10–1 and 10–2.

For all these results, the permeability coefficient is assumed to be constant by neglecting the inertial effect, and homogeneous to both directions throughout this research because of following reasons. The first is that the mass flow rate does not reach so high as shown in these figures under practical operating conditions. In addition, variations of 20 or 30 percent have little significant effects on the performance characteristics. Lastly, the variation of the permeability coefficient can be included in the variation of the permeability ratio.

Permeability Ratio γ

The surface of the porous metal facing the bearing gap is ground not only to get a smooth surface but also to improve the bearing characteristics. In this paper, the loading effect is estimated by adopting the permeability ratio γ. The effects of the permeability ratio are mentioned in the theoretical results and discussion.

Values of the permeability ratio are obtained experimentally. Figs. 23 and 24 show the relations between γ and pressure. The problem is that γ is described as the function of $P_s^2-P_b^2$. To simplify this treatment, the values of γ are read from the relations by assuming $P_b=P_a=1$. Thus, the obtained γ will provide a well estimated value where the pressure in the bearing gap nears the ambient

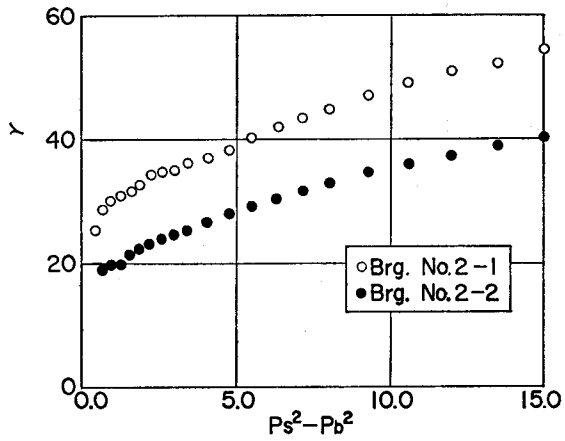

Fig. 23. Measured permeability ratio, (i).

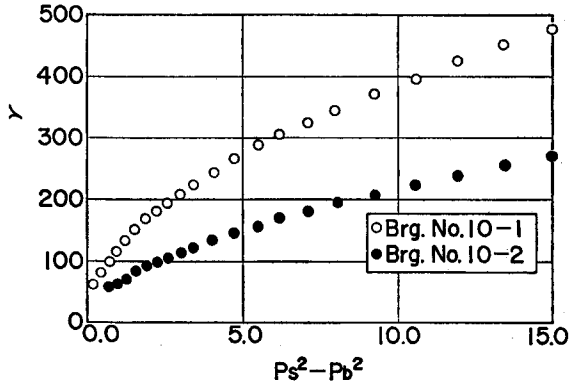

Fig. 24. Measured permeability ratio, (ii).

pressure. On the other hand, it may show an overestimated value where the pressure difference is comparatively small. The reason for applying this value is that the mass flow rate at a small pressure difference is, in fact, of less significance compared with the rate at a high pressure difference.

3.2 Experimental Procedure and Apparatus

The experimental apparatus is shown in Fig. 25. Journal (4) is supported by thrust bearing (1), journal bearing (2) and back pressure (3). Compressed gas is fed to (1), (2) and (3) respectively. Thickness of the bearing gap can be

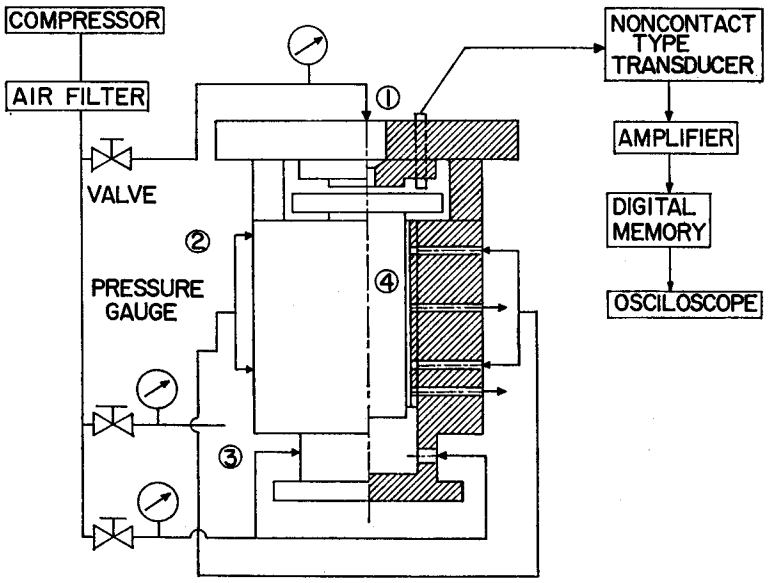

Fig. 25. Experimental apparatus.

varied by controlling the supply pressure and the back pressure. After the thickness is adjusted, impulse load is given on the head of the journal.

The frequency and amplitude are measured through a non-contact type transducer, digital memory and oscilloscope. The values of frequency f and logarithmic decrement δ are put in eqs. (3.1) and (3.2) to yield actual stiffness and damping coefficient.

$$k^* = mf^2(4\pi^2+\delta^2) \tag{3.1}$$

$$c = 2mf\delta \tag{3.2}$$

The dimensionless stiffness and damping coefficient are defined in eqs. (2.25) and (2.26). The actual load capacity is obtained by knowing the mass of the journal and the back pressure, and its dimensionless form is available by defining

$$W = \frac{w}{\pi r_0^2(p_s-p_a)} \tag{3.3}$$

The dimensions of the test bearings are shown in Table 2.

Table 2.

Brg. No.	k (cm^2)	γ (P_s=2.0)	γ (P_s=3.0)	R_1	R_2	r_0 (cm)	l (cm)
2–1	1.59×10^{-8}	35.1	43.2	0.8	0.18	2.8	0.5
2–2	1.80×10^{-8}	24.4	32.9	0.8	0.18	2.8	0.5
10–1	7.81×10^{-8}	209.7	345.6	0.8	0.18	2.8	0.5
10–2	8.00×10^{-8}	114.2	194.2	0.8	0.18	2.8	0.5

3.3 Experimental Results and Discussion

The relations between the load capacity and the bearing gap are shown in Figs. 26–29. The experimental results show a good agreement with the theoretical results. In some cases, the experimental results show slightly lower values than the theoretical results.

The dynamic stiffness and damping coefficients are obtained in relation to the bearing gap. They are shown in Figs. 30–37.

As for K, the theoretical and experimental results show a good agreement at comparatively high values of the actual gap h. One may admit an indication of improvement at the small values of h. However, another peak expected theoretically is not observed. An overestimation of the effect of the squeeze action is considered to be responsible for these results.

As for B, the experimental results show a good accordance with the theoretical results for the comparatively high values of γ, and tend to show lower values than expected for the P_s=2.0 case.

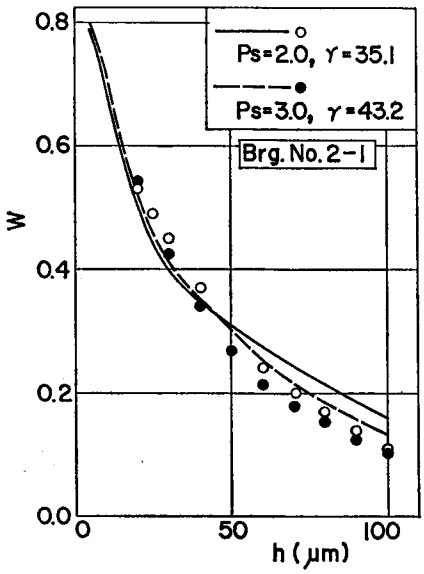

Fig. 26. Load capacicity, (i).

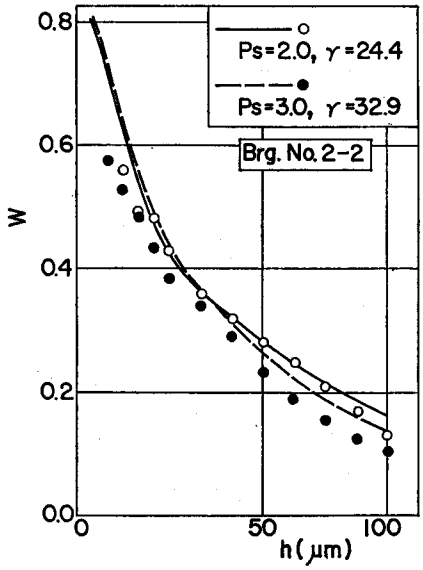

Fig. 27. Load capacity, (ii).

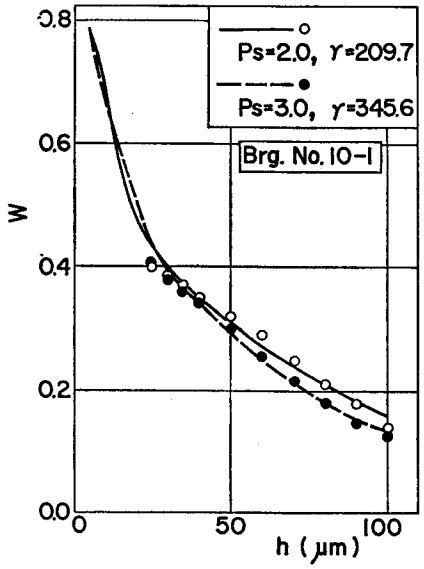

Fig. 28. Load capacity, (iii).

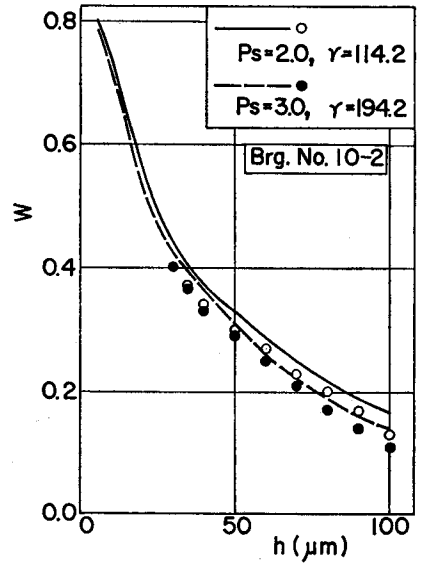

Fig. 29. Load capacity, (iv).

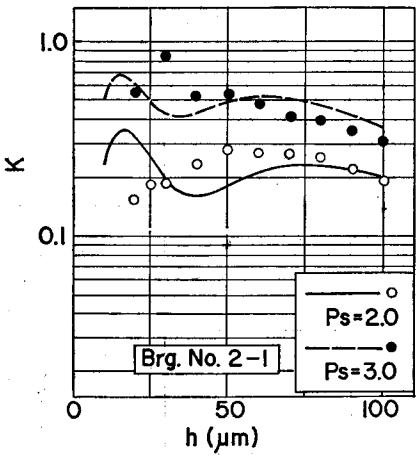

Fig. 30. Dynamic stiffness *vs.* bearing gap, (i).

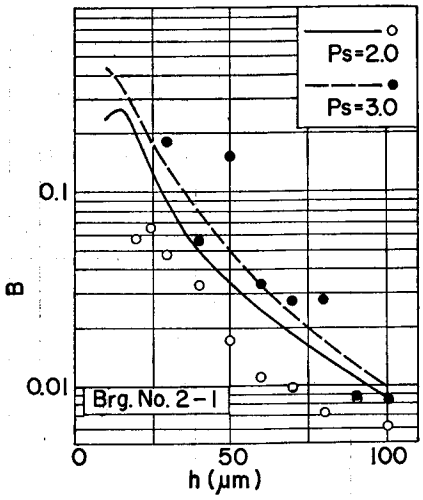

Fig. 31. Damping coefficient *vs.* bearing gap, (i).

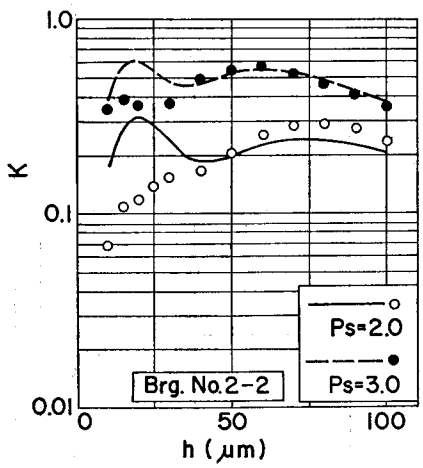

Fig. 23. Dynamic stiffness *vs.* bearing gap, (ii).

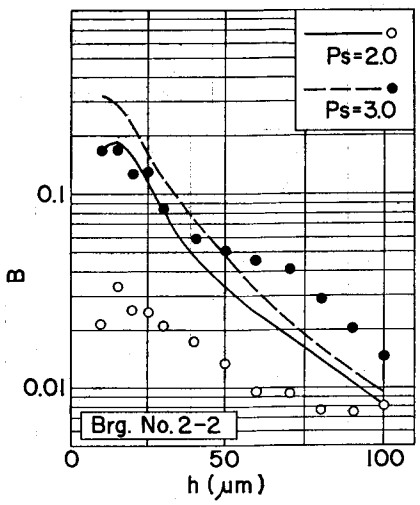

Fig. 33. Damping coefficient *vs.* bearing gap, (ii).

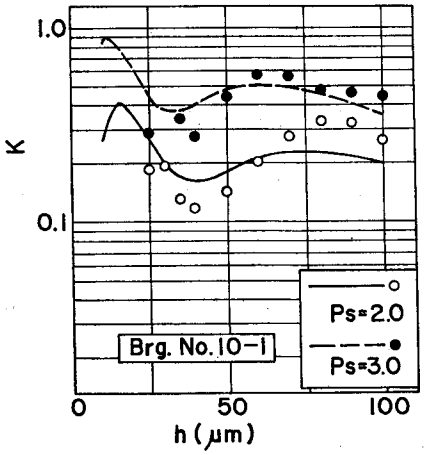

Fig. 34. Dynamic stiffness *vs.* bearing gap, (iii).

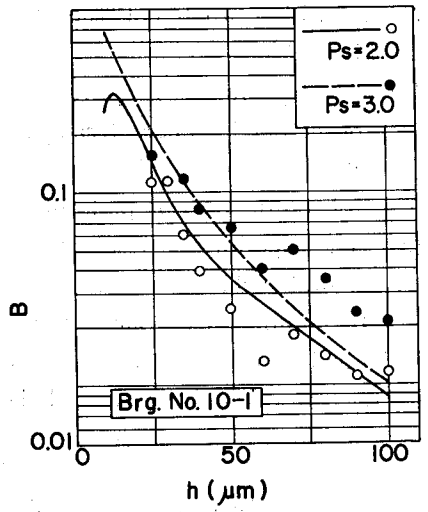

Fig. 35. Damping coefficient *vs.* bearing gap, (iii).

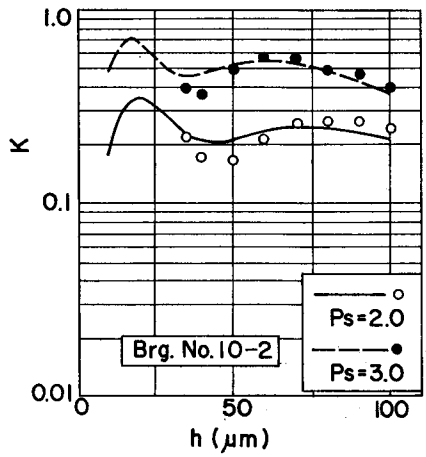

Fig. 36. Dynamic stiffness *vs.* bearing gap, (iv).

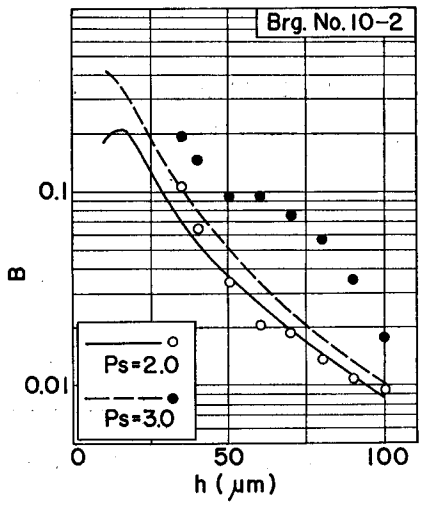

Fig. 37. Damping coefficient *vs.* bearing gap, (iv).

Closer examinations are expected especially on these points. One of the points is that the performance at the small gap should be treated more precisely. The other point is the effect of the locality of the permeability ratio on the bearing performance.

4. Conclusions

In this paper, the caracteristics of the externally pressurized porous thrust

bearing with a supply hole is examined. The following conclusions were obtained by this research.

(1) The hypothesis of equivalent film thickness provides satisfactory predictions of the bearing characteristics.

(2) Both the permeability coefficient and the permeability ratio play an important role on the bearing performance.

(3) The experimental results have proved that this hybrid-type bearing can give desirable characteristics.

In addition, dynamic performances are calculated with respect to various designing parameters. These results may allow the designers to choose adequate parameters which give optimal design conditions.

References

1) Mori, H., Yabe, H., and Ono, T., Trans. JSME, 29, 205 (1963), 1466.
2) Mori, H., Yabe, H., Trans. ASME, Ser. F, 95, 2 (1973), 195.

Appendixes

Appendix 1 Method of evaluating permeability coefficient, k.

(1) z-direction (Fig. a)

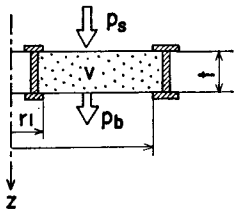

Fig. a. Measurement of K in z-direction.

For the flow to the z-direction, eq. (2.1) is applicable, then

$$\rho v = -\frac{1}{2RT}\frac{k}{\mu}\frac{dp^2}{dZ} \tag{A1.1}$$

This equation is integrated once to yield

$$k = \frac{2RT\cdot\mu}{A}\frac{t}{p_s^2-p_b^2}\cdot\dot{m} \tag{A1.2}$$

where $A=\pi(r_0^2-r_1^2)$

(2) r-direction (Fig. b)

Similarly, eq. (2.2) is applied,

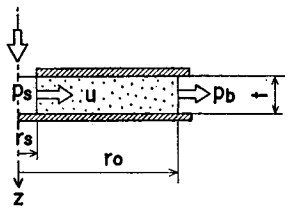

Fig. b. Measurement of K in r-direction.

$$\rho u = -\frac{1}{2RT}\frac{k}{\mu}\frac{dp^2}{dr} \tag{A1.3}$$

$$k = \frac{RT\cdot\mu}{\pi t}\frac{1}{p_s^2-p_b^2} ln\ \frac{r_0}{r_s}\cdot\dot{m} \tag{A1.4}$$

Appendix 2 Method of evaluating permeability ratio, γ.

Region I and Region II are defined as shown in Fig. c.

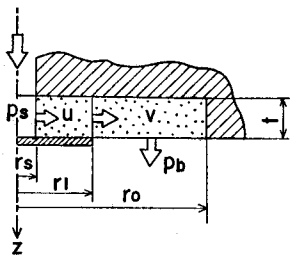

Fig. c. Measurement of γ.

(1) Region I ($r_s \leq r \leq r_1$)

For the flow to the r-direction, eq. (A1.1) is also applied,

$$p^2 = p_s^2 - \frac{RT}{\pi t}\frac{\mu}{k} ln\ \frac{r}{r_s}\cdot\dot{m} \tag{A2.1}$$

(2) Region II ($r_1 \leq r \leq r_0$)

The time dependent factor in eq. (2.9) is eliminated to yield,

$$\frac{p^2-p_a^2}{\eta} = t\left(\frac{1}{r}\frac{dp^2}{dr}+\frac{d^2p^2}{dr^2}\right) \tag{A2.2}$$

These equations are solved analytically by applying the following boundary conditions.

$$p|_{r=r_1}\ (\text{Region I}) = p|_{r=r_1}\ (\text{Region II}) \tag{A2.3}$$

$$\left.\frac{dP^2}{dr}\right|_{r=r_1}\ (\text{Region I}) = \left.\frac{dP^2}{dr}\right|_{r=r_1}\ (\text{Region II}) \tag{A2.4}$$

$$\left.\frac{dP^2}{dr}\right|_{r=r_0} = 0 \tag{A2.5}$$